

# Magic angle in thermal conductivity of twisted bilayer graphene

Yajuan Cheng,<sup>1</sup> Zheyong Fan,<sup>2</sup> Tao Zhang,<sup>1</sup> Masahiro Nomura,<sup>3</sup>  
Sebastian Volz,<sup>3</sup> Guimei Zhu,<sup>4,†</sup> Baowen Li,<sup>5,\*</sup> and Shiyun Xiong<sup>6,‡</sup>

<sup>1</sup>*School of Physics and Materials Science, Guangzhou University, Guangzhou 510006, China*

<sup>2</sup>*College of Physical Science and Technology, Bohai University, Jinzhou 121013, P. R. China*

<sup>3</sup>*Laboratory for Integrated Micro Mechatronic Systems (LIMMS/CNRS-IIS),*

*The University of Tokyo, Tokyo 153-8505, Japan*

<sup>4</sup>*School of Microelectronics, Southern University of Science and Technology, Shenzhen 518055, China*

<sup>5</sup>*Department of Materials Science and Engineering, Department of Physics,*

*Southern University of Science and Technology, Shenzhen 518055, China*

*Paul M. Rady Department of Mechanical Engineering and Department of Physics,*  
*University of Colorado, Boulder, Colorado 80305-0427, USA*

<sup>6</sup>*Guangzhou Key Laboratory of Low-Dimensional Materials and Energy Storage Devices,*  
*School of Materials and Energy, Guangdong University of Technology, Guangzhou 510006, China*

In this Letter, we report a magic angle of  $1.08^\circ$  in the thermal conductivity of twisted bilayer graphene (TBLG). Within the supercell of a moiré lattice, there exist sites with different stacking modes between the two graphene layers, which serve as scatterers for the phonons that reduce the thermal conductivity of TBLG compared to that of untwisted bilayer graphene. Our detailed study reveals that the thermal magic angle arises from the competition between the weakened spatial dependence of vibrational amplitude and stress on one hand, and the increased number of scattering sites on the other hand. The rapid decrease of spatial mismatch for atomic vibrational amplitudes and local stresses at small angles significantly weakens the scattering strength of a single scatterer. In contrast, the reduced crystal period with twist angle dramatically increases scatterer density. The combination of the two effects eventually leads to the apparition of this irregularity in heat conduction. Our work not only enriches the research of twisted graphene, but also reveals the underlying physics of the thermal magic angle, which should impact heat conduction in two-dimensional materials in general.

Twisted bilayer graphene (TBLG) exhibits a moiré pattern with a larger second lattice periodicity. When the twist angle between the two graphene layers reaches  $1.08^\circ$ , which called magic angle [1–3], band hybridization and avoided crossings emerge and result in the formation of flat bands near the Dirac point. This unusual behavior leads to many novel phenomena that are not prevalent either in a single-layer or in a bilayer graphene. Among many others are electronic correlation, superconductivity, spontaneous ferromagnetism, quantized anomalous Hall states, and topologically protected states. This magic angle has attracted substantial research interests in recent years since its theoretical prediction and experimental observation [4–13].

In this work, we report an abnormal behavior of thermal property in the vicinity of  $1.08^\circ$ , where the thermal conductivity shows a local dip. Our systematic investigations with homogeneous non-equilibrium molecular dynamic (HNEMD) simulations reveal that the magic arises from the competition between the reduced spatial dependence of atomic vibrational amplitude and stress on one side, and the increased density of scattering sites on the other side. The former weakens the scattering effect of a single site while the latter strengthens the scattering rates.

The Moiré lattice formed in TBLG has a lattice parameter that decreases with increasing twist angle  $\theta$  as  $a_{\text{moire}} = \frac{a}{2\sin(\theta/2)}$ ,  $a = 2.452 \text{ \AA}$  being the lattice param-

eter of monolayer graphene. The unit cell of the Moiré lattice has an hexagonal shape as shown by the black lines in the top panel of Fig. 1. Inside the unit cell of the Moiré lattice, the stacking between the two layers is not uniform. Typical stacking modes include AA stack, AB stack, and SP stack, which are schematically illustrated in the bottom panel of Fig. 1.

To construct an orthogonal simulation box, we adopted a larger unit cell with a rectangle shape as indicated by the blue dashed lines in Fig. 1. The number of atoms in such a rectangular cell is twice that in the hexagonal unit cell. To simulate the thermal transport properties of TBLG, we performed HNEMD simulations [14, 15] implemented in the graphics processing units molecular dynamics (GPUMD) package [16]. The intralayer C-C interaction is described by the optimized Tersoff potential [17] while the interlayer C-C interaction is governed by the interlayer potential (ILP) [18]. The ILP potential has been proven to provide a better description for the interlayer weak Van der Waals interactions than the commonly used Lennard-Jones (LJ) potential as demonstrated by Lebedeva *et al* [18]. The cutoff of the ILP potential is chosen as  $15 \text{ \AA}$ , beyond which atomic interaction energies are negligible. During the simulations, a time step of  $1.0 \text{ fs}$  is adopted for the integration of Newton's equation. The details of HNEMD formulation as well as the decomposition of the TC into the in-plane and out-of-plane modes can be found in the supplement

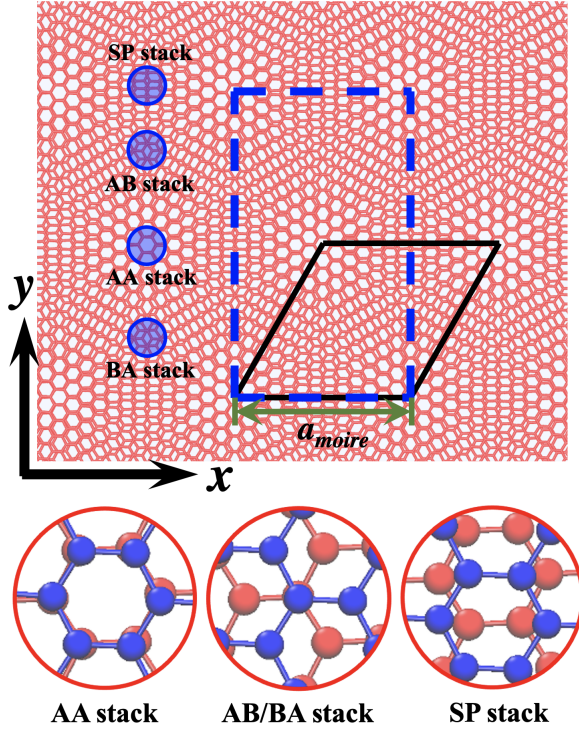


FIG. 1. Top panel: the Moiré lattice formed in TBLG. The relative position of AA, AB, and SP stacks are illustrated by the circles and the unit cell of the Moiré lattice is indicated by the black parallelogram. Bottom panel: the atomic arrangements of AA, AB, and SP stacks. Red and blue atoms correspond to the atoms in the bottom and top layers, respectively.

tary material.

Fig. 2(a) illustrates the twisted angle dependent thermal conductivity (TC) at 300 K. In general, the TC of TBLG is reduced compared to the untwisted one. Below  $1.08^\circ$ , the TC decreases rapidly with the increase of twist angle. While beyond  $10^\circ$ , the TC slightly increases, which is in agreement with other simulations [19–21] and experiments [22, 23]. Surprisingly, we observe an abnormal TC valley in the vicinity of  $1.08^\circ$ . Beyond that the TC increases rapidly and reach a local maximum when the angle reaches around  $3^\circ$ . After that the TC decreases.

It is well known that  $1.08^\circ$  corresponds to the magic angle for electron transport, at which superconductivity emerges at low temperatures [2, 3]. Thus we call this angle - thermal magic angle. What is the underlying mechanism of this coincidence?

Our study shows that the thermal magic angle also emerges at other temperatures as shown in Fig. 2(c) and (d). Moreover, to verify whether the thermal magic angle is related to the adopted interlayer potential, we also calculated the TC of TBLG with the LJ potential. The results emphasize that an abnormal TC increase starting from  $1.56^\circ$  is also preserved (Fig. S2). Therefore, we believe that the observed thermal magic angle is an

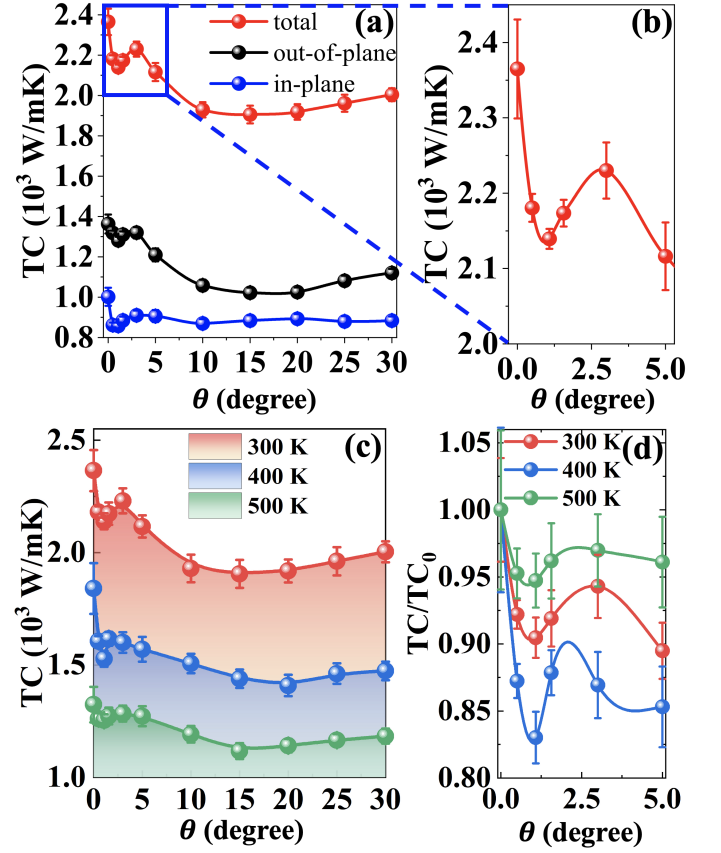


FIG. 2. (a) Total, in-plane, and out-of-plane thermal conductivity of TBLG as a function of twist angle from  $0^\circ$  to  $30^\circ$  at 300 K. (b) Total thermal conductivity of TBLG with twist angle below  $5^\circ$ . (c) Total thermal conductivity of TBLG versus with twist angle at different temperature: 300 K, 400 K, and 500 K. (d) Normalized thermal conductivity with respect to the value of untwisted structure as a function of twist angle at 300 K, 400 K, and 500 K.

intrinsic property of TBLG.

For two-dimensional materials, the in-plane and out-of-plane modes contribute much differently to the total TC [24]. To examine such a difference and the effect of the twist angle on the in-plane and out-of-plane modes, we decompose the total TC into the contributions of in-plane and out-of-plane modes at 300 K following the method proposed in Ref. 15. The corresponding results are reported in Fig. 2(a). Similarly to other two-dimensional materials, the out-of-plane modes contribute more to the total TC than the in-plane ones. Interestingly, the in-plane TC is more sensitive to the twist angle below  $1.08^\circ$  while remaining almost constant beyond  $3^\circ$ . As a result, the in-plane TC around  $1.08^\circ$  corresponds to the global minimum. In contrast, the out-of-plane TC rapidly decreases from  $3^\circ$  to  $10^\circ$ . Moreover, the total TC increase beyond  $15^\circ$  is fully contributed by the out-of-plane modes.

In the following, we shall illustrate that the magic ther-

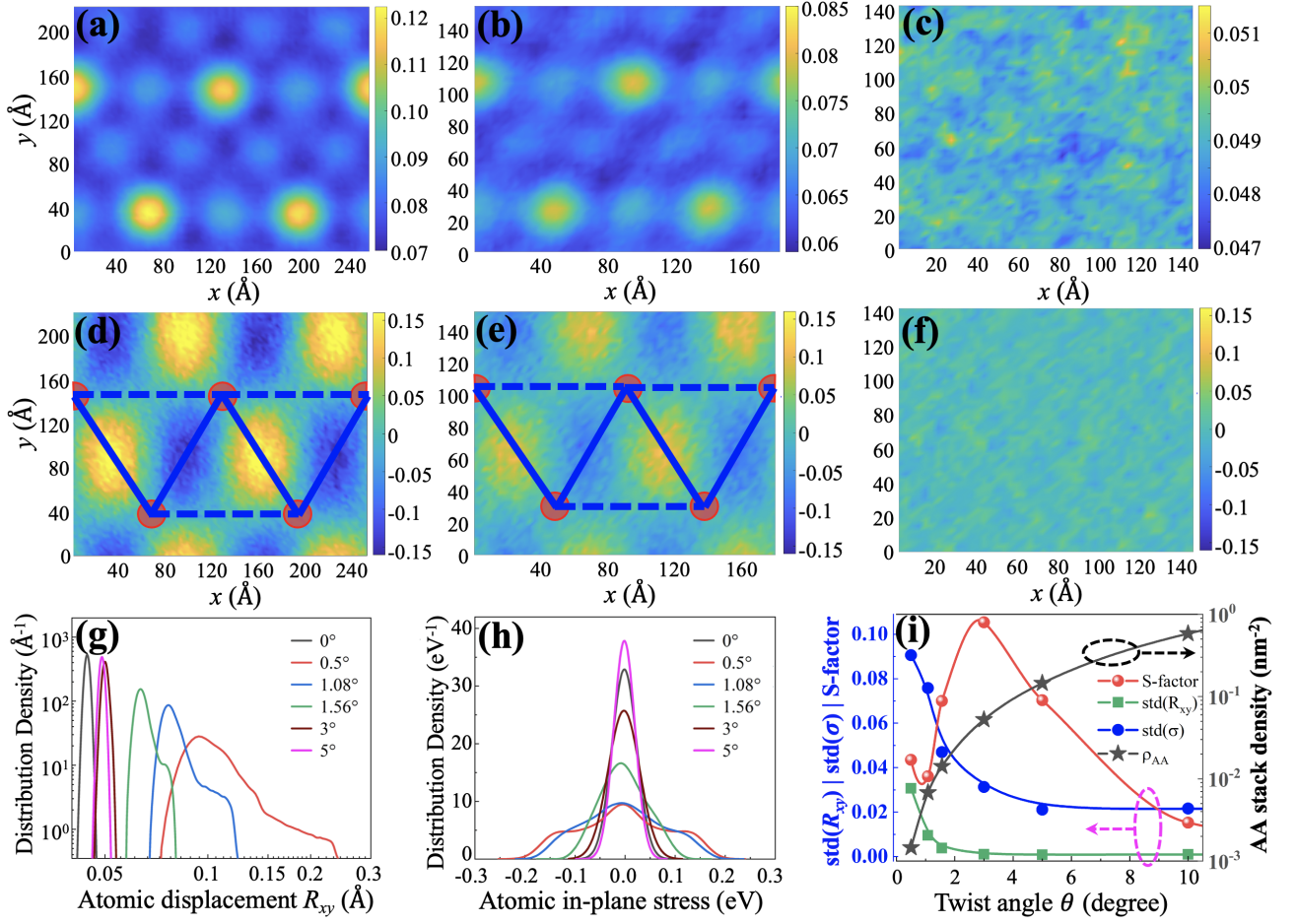


FIG. 3. Spatial distribution of in-plan atomic vibrational amplitude at (a)  $\theta = 1.08^\circ$ , (b)  $\theta = 1.56^\circ$ , and (c)  $\theta = 5.0^\circ$  (unit:  $\text{\AA}$ ). The bright yellow regions correspond to AA stacks in (a) and (b). Spatial distribution of atomic (normal) stress along the  $x$  direction ( $\sigma_{xx}$ ) of the bottom graphene layer for (d)  $1.08^\circ$ , (e)  $1.56^\circ$ , and (f)  $5^\circ$  at 300 K (unit: eV). The red disks denote the AA stack centers. The averaged stress for all systems is shifted to zero. (g) the atomic in-plane vibrational amplitude distribution at different angles. (h) the distribution of atomic normal stress for all atoms at indicated angles. (i) Twist angle dependent S-factor in TBLG calculated by Eq. 1. The constant  $C$  is chosen as  $6 \times 10^{-6} \text{ \AA eV/nm}^2$  to make the value of S-factor in the same range of  $\text{std}(\sigma)$ .

mal property is due to the competition between the reduced mismatch of local properties (atomic vibrational amplitude and stress) and increased scattering center density.

In TBLG, the Moiré unit cell is relatively large and the stacking is not uniform inside the unit cell. It changes from the stable AB stack to the unstable AA and SP stacks continuously (Fig. 1). Such a non-uniform stack can scatter phonons strongly, thus reducing the TC. On the other hand, it can also lead to spatial-dependent vibrational and mechanical properties, such as the atomic vibrational amplitude and the atomic stress. We will show that the thermal magic angle arises from the interplay between the increased number of scattering centers on one side, and the weakened spatial-dependent atomic vibrational amplitude and stress on the other side.

At zero temperature, the AA stack has a larger equi-

librium interlayer distance ( $3.65 \text{ \AA}$ ) compared to the one of the AB stack ( $3.38 \text{ \AA}$ ) (Fig. S3). For small twist angles, the AA and AB stack centers are far away from each other, and the interlayer distances around AA and AB centers highlight distinct differences (Fig. S4). With the increase of  $\theta$ , the reduced AA and AB distances make their interlayer interactions around AA and AB regions more balanced. Therefore the interlayer distance becomes less spatial dependent (Fig. S4). The spatial dependent interlayer distance (especially at small angles) affect the atomic vibrations in different regions. To examine those, we analyze the atomic trajectories for each case. Due to the fluctuations of TBLG in the out-of-plane direction ( $z$ ), we only count the atomic displacement along the in-plane directions ( $x$  and  $y$ ).

Figs. 3(a)-(c) report the time-averaged atomic in-plane vibration amplitude  $R_{xy}$  at  $1.08^\circ$ ,  $1.56^\circ$  and  $5^\circ$  (300 K).



At small angles, the spatial distribution of  $R_{xy}$  clearly represents the Moiré patterns, where  $R_{xy}$  is maximized at the AA stack regions. The mismatch magnitude of the vibrational amplitudes at different regions reduces rapidly as the twist angle increases. In Fig. 3(g), the distribution range of  $R_{xy}$  is large at small angles but reduces rapidly with the increase of the twist angle. Starting from  $3^\circ$ ,  $R_{xy}$  becomes a normal distribution with a small standard deviation, which is similar to the one of the untwisted structure. The averaged  $R_{xy}$  at  $\theta \geq 3^\circ$  is reaching  $0.05\text{\AA}$ , which is slightly larger than the corresponding value of the untwisted structure (Fig. S7).

Similarly to  $R_{xy}$ , we find that the in-plane atomic stress is also spatial dependent because the rotation changes the periodicity of graphene along a specific spatial direction, leading to different period lengths along the same direction for the top and bottom layers. The lattice mismatch can cause the atoms from the top and bottom layers to attract or repel each other along a specific in-plane direction. Since the attraction and repulsion occur between the two layers, the stresses of the top and bottom layers are directed in opposite directions with similar magnitudes at the same place (Fig. S8).

Fig. 3(d)-(f) illustrates the time-averaged normal stress along the  $x$  direction (i.e.,  $\sigma_{xx}$ ) of the bottom layer graphene for  $\theta = 1.08^\circ$ ,  $1.56^\circ$  and  $5^\circ$ , respectively, for temperature at 300 K. Different from The maximum/minimum of vibrational amplitudes that are located at the AA or AB stack, the maximum and minimum of the stresses are located between the two neighboring AA regions.

Due to the symmetry of the TBLG, the maximum/minimum of the normal stresses  $\sigma_{xx}$  and  $\sigma_{yy}$  are located at two edges of the triangle formed by AA centers (solid lines in Fig. 3(d)), while another edge of the triangle (dashed line) possesses the maximum/minimum shear stress  $\tau_{xy}$  as shown in Fig. S11. At small twist angles, the atoms at different regions carry fairly different stresses. Such a local stress difference reduces rapidly with the increase of the twist angle and becomes negligible eventually.

To check the distribution of atomic stresses, we counted the distributions of  $\sigma_{xx}$  and  $\sigma_{yy}$  as shown in Fig. 3(h). It clearly shows that the stress is distributed in a broad range in the small twist angle region. For example,  $\sigma_{xx}$  and  $\sigma_{yy}$  are ranging from  $-0.2$  to  $0.2$  eV when  $\theta = 0.5^\circ$ . With the increase of  $\theta$ , the stress distribution range reduces and it becomes a normal distribution with reduced standard deviations starting from  $5^\circ$ , which is similar to the case of the untwisted structure (Fig. S10).

The structure-induced spatial inhomogeneity in TBLG can strongly scatter phonons, which induces the reduction of TC in bilayer graphene with a twist. Larger vibrational amplitudes result in stronger anharmonicity while local stresses can lead to the mismatch of phonon frequencies. The total phonon scattering strength depends

both on the scattering strength of each individual scatterer and the density of scatterers. In TBLG, the scattering strength of a single scatterer can be characterized by the standard deviation of the corresponding distribution function, namely  $\text{std}(R_{xy})$  and  $\text{std}(\sigma)$ . Since the number of stress and vibrational amplitude maxima/minima is directly related to the AA stack numbers, we use the AA stack density  $\rho_{AA}$  to represent the density of scatterers.

The variation of  $\rho_{AA}$ ,  $\text{std}(R_{xy})$  and  $\text{std}(\sigma)$  as a function of  $\theta$  are illustrated in Fig. S12. At small angles,  $\rho_{AA}$  increases dramatically with  $\theta$  while both  $\text{std}(R_{xy})$  and  $\text{std}(\sigma)$  decreases rapidly. The increased  $\rho_{AA}$  produces more scattering sites while the reduced  $\text{std}(R_{xy})$  and  $\text{std}(\sigma)$  weakens the scattering strength of a single scattering site. As a result, the two effects compete with each other and eventually lead to the abnormal TC increase after  $1.08^\circ$ . Here we can define a  $S$ -factor:

$$S = \frac{C}{\text{std}(R_{xy})\text{std}(\sigma)\rho_{AA}} \quad (1)$$

to quantify the effect of the scattering, where  $C$  is a constant. The denominator  $\text{std}(R_{xy})\text{std}(\sigma)\rho_{AA}$  characterizes the total scattering strength, i.e., the product of scattering strength of a single scatterer and site density of scatterers.

Fig. 3(i) illustrates the variation of  $S$ -factor with twist angle at 300 K. Interestingly, the twist angle dependent  $S$ -factor features the same trend as TC. Starting from  $0.5^\circ$ , the  $S$ -factor decreases first and reaches to a local minimum around  $1.08^\circ$ . With further increase of the twist angle, the  $S$ -factor increases and reaches to a local maximum around  $3^\circ$ . After that, it reduces with the increase of twist angle. The similar trend of  $S$ -factor and TC with the variation of twist angle quantitatively confirms the thermal magic arises from the interplay between the reduced scattering strength of a single scatterer and the increased scattering site density.

With the further increase of the twist angle after  $3^\circ$ , the weakening effect of the scattering strength of a single scattering site is negligible and the TC is governed by the increased scattering site density again, which leads to the TC decrease after  $3^\circ$ . We note that beyond  $10^\circ$ , the TC is slightly enhanced with the increase of the twist angle, which is related to a coherent phonon transport effect similar to case in superlattices [25–27].

Beyond  $10^\circ$ , all properties become spatial independent. The AA center distance also becomes very short ( $\sim 1.5$  nm at  $10^\circ$ ), which could be shorter than the size of some phonon wave packets. In such a situation, those phonons can not feel the scatterers and behave as the material would be a homogeneous structure. With the increase of  $\theta$ , more and more phonons travel coherently, which leads to the increase of TC with  $\theta$ .

It is worth noting that although both electronic magic angle and thermal magic angle happen at the same value,  $1.08^\circ$ , the underlying mechanisms are quite different. In

the electronic case, it is the strong electron correlation which happens only at extremely low temperature, at which lattice vibrations is extremely small and will not break down the electron correlations. In contrast, in the thermal case, it is due to atomic vibrations and the thermal magic can even exist at high temperatures as illustrated in our current work in Fig. 2.

In summary, we find a thermal magic angle at  $1.08^\circ$  at which a local dip of the thermal conductivity appears. The decomposition analysis of the thermal conductivity demonstrates that the rapid thermal conductivity reduction below  $1.08^\circ$  arises from the reduction of both in-plane and out-of-plane mode contributions. While beyond  $3^\circ$ , the thermal conductivity reduction arises mainly from the out-of-plane mode contribution. The twist of bilayer graphene leads to non-uniform stackings, which results in spatial-dependent properties and thus scatters phonons. At small angles, the space dependence of both vibrational amplitude and stress weakens with the increase of twist angle, leading to a reduced scattering strength of a single scatterer. On the other hand, the scattering sites dramatically increase in number with the twist angle. The competition between these two effects eventually result in the formation of a thermal magic angle. The current research could help to understand the origin of twist angle-dependent properties in TBLG, especially around the magic angle, and be beneficial for discovering other novel properties in TBLG. The physical mechanisms discovered will also provide clues for thermal management and control by using graphene and related materials.

## ACKNOWLEDGEMENTS

Y. Cheng and Z. Fan contribute equally to this work. This work was supported by the National Natural Science Foundation of China under Grant No. 12174276, the Major Research Plan of the National Natural Science Foundation of China (Grant No. 91833303), and the Major International (Regional) Joint Research Project of the National Natural Science Foundation of China (Grant No. 51920105005).

---

<sup>†</sup> E-mail: zhugm@mail.sustech.edu.cn

<sup>\*</sup> E-mail: libw@sustech.edu.cn

<sup>‡</sup> E-mail: xiongshiyun216@163.com

- [1] R. Bistritzer and A. H. MacDonald, *Proceedings of the National Academy of Sciences* **108**, 12233 (2011).
- [2] Y. Cao, V. Fatemi, S. Fang, K. Watanabe, T. Taniguchi, E. Kaxiras, and P. Jarillo-Herrero, *Nature* **556**, 43 (2018).
- [3] Y. Cao, V. Fatemi, A. Demir, S. Fang, S. L. Tomarken, J. Y. Luo, J. D. Sanchez-Yamagishi, K. Watanabe, T. Taniguchi, E. Kaxiras, R. C. Ashoori, and P. Jarillo-Herrero, *Nature* **556**, 80 (2018).
- [4] L. Huder, A. Artaud, T. Le Quang, G. T. de Laissardière, A. G. M. Jansen, G. Lapertot, C. Chapelier, and V. T. Renard, *Phys. Rev. Lett.* **120**, 156405 (2018).
- [5] M. Koshino, N. F. Q. Yuan, T. Koretsune, M. Ochi, K. Kuroki, and L. Fu, *Phys. Rev. X* **8**, 031087 (2018).
- [6] M. Oh, K. P. Nuckolls, D. Wong, R. L. Lee, X. Liu, K. Watanabe, T. Taniguchi, and A. Yazdani, *Nature* **600**, 240 (2021).
- [7] D. E. Parker, T. Soejima, J. Hauschild, M. P. Zaletel, and N. Bultinck, *Phys. Rev. Lett.* **127**, 027601 (2021).
- [8] J. M. Park, Y. Cao, K. Watanabe, T. Taniguchi, and P. Jarillo-Herrero, *Nature* **590**, 249 (2021).
- [9] A. Kerelsky, L. J. McGilly, D. M. Kennes, L. Xian, M. Yankowitz, S. Chen, K. Watanabe, T. Taniguchi, J. Hone, C. Dean, A. Rubio, and A. N. Pasupathy, *Nature* **572**, 95 (2019).
- [10] L. Sharpe Aaron, J. Fox Eli, W. Barnard Arthur, J. Finney, K. Watanabe, T. Taniguchi, M. A. Kastner, and D. Goldhaber-Gordon, *Science* **365**, 605 (2019).
- [11] Y. Shimazaki, I. Schwartz, K. Watanabe, T. Taniguchi, M. Kroner, and A. ImamoAlu, *Nature* **580**, 472 (2020).
- [12] X. Lu, P. Stepanov, W. Yang, M. Xie, M. A. Aamir, I. Das, C. Urgell, K. Watanabe, T. Taniguchi, G. Zhang, A. Bachtold, A. H. MacDonald, and D. K. Efetov, *Nature* **574**, 653 (2019).
- [13] S. Zhang, Q. Xu, Y. Hou, A. Song, Y. Ma, L. Gao, M. Zhu, T. Ma, L. Liu, X.-Q. Feng, and Q. Li, *Nature Materials* (2022), 10.1038/s41563-022-01232-2.
- [14] D. J. Evans, *Physics Letters A* **91**, 457 (1982).
- [15] Z. Fan, H. Dong, A. Harju, and T. Ala-Nissila, *Phys. Rev. B* **99**, 064308 (2019).
- [16] Z. Fan, W. Chen, V. Vierimaa, and A. Harju, *Computer Physics Communications* **218**, 10 (2017).
- [17] L. Lindsay and D. A. Broido, *Phys. Rev. B* **81**, 205441 (2010).
- [18] I. V. Lebedeva, A. A. Knizhnik, A. M. Popov, Y. E. Lozovik, and B. V. Potapkin, *Physical Chemistry Chemical Physics* **13**, 5687 (2011).
- [19] X. Nie, L. Zhao, S. Deng, Y. Zhang, and Z. Du, *International Journal of Heat and Mass Transfer* **137**, 161 (2019).
- [20] M.-H. Wang, Y.-E. Xie, and Y.-P. Chen, *Chinese Physics B* **26**, 116503 (2017).
- [21] C. Li, B. Debnath, X. Tan, S. Su, K. Xu, S. Ge, M. R. Neupane, and R. K. Lake, *Carbon* **138**, 451 (2018).
- [22] H. Li, H. Ying, X. Chen, D. L. Nika, A. I. Cocemasov, W. Cai, A. A. Balandin, and S. Chen, *Nanoscale* **6**, 13402 (2014).
- [23] S. Han, X. Nie, S. Gu, W. Liu, L. Chen, H. Ying, L. Wang, Z. Cheng, L. Zhao, and S. Chen, *Applied Physics Letters* **118**, 193104 (2021).
- [24] X. Gu, Y. Wei, X. Yin, B. Li, and R. Yang, *Rev. Mod. Phys* **90**, 041002 (2018).
- [25] S. Xiong, B. Latour, Y. Ni, S. Volz, and Y. Chalopin, *Phys. Rev. B* **91**, 224307 (2015).
- [26] N. Luckyanova Maria, J. Garg, K. Esfarjani, A. Jandl, T. Bulsara Mayank, J. Schmidt Aaron, J. Minnich Austin, S. Chen, S. Dresselhaus Mildred, Z. Ren, A. Fitzgerald Eugene, and G. Chen, *Science* **338**, 936 (2012).
- [27] B. Latour and Y. Chalopin, *Phys. Rev. B* **95**, 214310 (2017).